ABSTRACT

SAMBAMURTHY, VIVEK SUBRAMANIAM. Array Jet Impingement on High Porosity Thin Metal Foams: Effect of Foam Height, Pore-Density and Spent Air Crossflow Scheme on Flow Distribution and Heat Transfer. (Under the direction of Dr. Srinath V. Ekkad).

An experimental investigation was carried out to study heat transfer and fluid flow in high porosity (93%) thin metal foams subjected to array jet impingement, under maximum and intermediate crossflow exit schemes. Separate effects of pore-density (pores per inch: PPI) and jet-to-target spacing (z/d) have been studied. To this end, for a fixed pore-density of 40 PPI foams, three different jet-to-target spacing (z/d=1, 2, 6) were investigated, and for a fixed jet-to-target spacing (z/d) of 6, three different pore-density of 5, 20 and 40 PPI were investigated. The jet diameter-based Reynolds number was varied between 3,000 and 12,000. Both flow and heat transfer experiments were carried out to characterize the flow distribution, crossflow mass flux accumulation and local Nusselt numbers for different jet impingement configurations. The heat transfer results were obtained through steady-state experiments. Local flow measurements show that, as jet-to-target distance decreases, the mass flux distributions are increasingly skewed with higher mass flow rates near the exits. Heat transfer enhancement has been calculated and the optimum foam configuration has been deduced from the pumping power required to achieve the enhancement. It was observed that Nusselt number increases with increasing pore density at a fixed jet-to-target spacing and reduces with increase in jet to target spacing at constant pore density. Intermediate crossflow had higher heat transfer than maximum crossflow with significantly lower pumping power. Under a constant pumping power condition, z/d = 2, 40 ppi foam produced an average enhancement of 35% over the corresponding baseline configuration for intermediate crossflow scheme and was found to be the most optimum configuration.

Keywords: metal foam; jet impingement.

Array Jet Impingement on High Porosity Thin Metal Foams: Effect of Foam Height, Pore-Density and Spent Air Crossflow Scheme on Flow Distribution and Heat Transfer.

by
Vivek Subramaniam Sambamurthy

A thesis submitted to the Graduate Faculty of
North Carolina State University
in partial fulfillment of the
requirements for the degree of
Master of Science

Mechanical Engineering

Raleigh, North Carolina
2020

APPROVED BY:

_____	_____
Dr. Srinath V. Ekkad Committee Chair	Dr. Alexei Saveliev
_____	
Dr. Tarek Echekki	

DEDICATION

To my family

BIOGRAPHY

Vivek Subramaniam Sambamurthy was born and raised in India. He graduated with a Bachelor's degree in Mechanical Engineering from National Institute of Technology, Tiruchirappalli (NITT) in the year 2018. To further his education, he moved to the United States of America to pursue Graduate Studies at North Carolina State University from fall 2018.

ACKNOWLEDGEMENTS

I would like to thank Dr. Srinath Ekkad for giving me the opportunity to work under him and for his unwavering support. His valuable guidance and expert advices have contributed immensely towards my holistic growth. He has always been and will continue to be a source of inspiration to me. I would also like to thank Dr. Alexei Saveliev and Dr. Tarek Echekki for being members in my committee.

Special thanks to Dr. Prashant Singh for all his thoughtful discussions, valuable insights and continuous encouragement throughout my time at the Thermal Energy Research and Management (ThERM) lab. This work would not have been possible without his support and inputs. Many thanks to Srivatsan for being my mentor throughout my master's journey. He has been available at all times to clear my doubts and has always been a constant source of motivation. I would also like to thank my lab mates Kishore, Sanskar, Pratik, Shoaib, Varun and Ramaswamy for their continuous support and making this journey memorable and joyful. I thank my roommates Ramaswamy and Siddarth for their understanding. I whole heartedly thank my friends from NIT Trichy and my friends here at NC State.

My heartfelt thanks to my parents Kalyani and Sambamurthy for being pillars of strength, who have always backed my decisions with utmost encouragement. I would also like to thank my grandmother for her prayers and blessings that has always given me a lot of positivity.

TABLE OF CONTENTS

LIST OF TABLES

LIST OF FIGURES

CHAPTER 1

Introduction and Background

Recent developments in the processing technology have led to production of a wide range of lightweight materials to be used for structural, thermal, acoustic among other engineering applications. Metal foams is one such unique porous material that finds wide ranging applications in the thermal management, aerospace and manufacturing industries. A metal foam is a cellular structure consisting of a solid base metal (e.g.: Aluminum, Copper) with gas-filled pores consisting of a large portion of the volume. The pores can be sealed (closed-cell foam) or interconnected (open-cell foam). The defining property of a metallic foam is the high porosity, ratio of volume of a void to the total volume, which is about 0.8-0.95, making them different from other porous materials.

On the other hand, there are multiple thermal management issues that needs improved cooling performance to mitigate the heat dissipated. One such field would be the electronics industry. The electronics industry is one of the fastest growing industries in the world with an increasing demand to augment computational processing speed while also keeping a check on the size of the system. This has led to high heat dissipation ($> 50\ W/cm^2$) at the chip level. The high level of heat fluxes has presented us, Thermal Engineers, the challenge of developing novel cooling strategies to effectively transport heat away from the components to ensure smooth functioning of the electronic systems. The research aims to address this challenge by using metal foams as heat transfer enhancement materials focused on electronic cooling application.

1.1 Trends in Electronic Cooling

The field of electronics involves construction and utilization of devices that involve flow of current through a vacuum, gas or a semiconductor [1]. Essentially, this current flow is through a resistance element and is always accompanied by heat generation (I^2R). The heat generation leads to rise in temperature of the component and often these components have a maximum operation temperature beyond which the performance starts to drop. Electronics cooling deals with cooling of a range of heat dissipating systems like phones, tablets, computers, data centers to electronic devices installed in airplanes, satellites, radars, etc. As a thermal engineer involved in cooling of electronics, our aim is to ensure that the component is within the working temperature and heat is dissipated effectively. Electronics cooling depends upon a variety of factors with size of the component and heat flux generated being the dominant factors. The most efficient cooling method would be one that does the required job at the lowest cost possible and occupying minimum space as well.

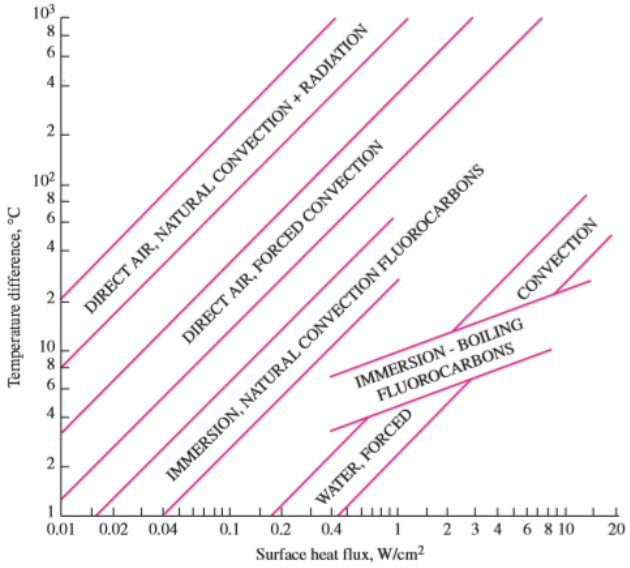

Figure 1.1: Heat fluxes that can be attained at specified temperature differences with various heat transfer mechanisms [2]

The heat fluxes attainable at specified temperature differences are plotted in Figure 1.1 for some common heat transfer mechanisms. When the power rating of the device is known, the flux is determined by dividing the rated power by surface area exposed after which suitable heat transfer mechanisms are selected. For example, a heat flux of $0.5\ W/cm^2$ from an electronic component would result in a temperature difference of about $500℃$ when only natural convection and radiation is used. Considering that maximum allowable temperature would be $\sim 80℃$, a better alternative compared to natural convection must be used. Modern cooling of electronics involves combining different heat transfer mechanisms to effectively enhance heat transfer. For example, modern computers use a heat pipe to transport heat from the component to a heat sink for which forced convection using air is used to cool down the heat sink. In this application, a heat pipe involves phase change heat transfer, conduction cooling as well as forced convection by air leading very efficient heat transfer. In this study, metal foams are used as heat sinks to conduct heat from the base plate and forced convection using air is used transport heat off from the metal foams.

1.2 Thermal transport in metal foams

Thermal transport in metal foams has received growing attention in academic as well as industrial applications. This section presents a brief background as to why metal foams are used in heat transfer applications and highlights various applications of metal foams. High porosity open cell metal foams have emerged as promising materials for thermal management applications where a large amount of heat needs to be transported over a small volume. The high surface area to volume ratio as well as enhanced flow mixing due to tortuous flow paths attributes to enhanced heat transfer [3]. The surface area density of metal foams is roughly $500 - 5000\ m^2/m^3$. Further, these metal foams can be processed in large quantities at low cost via metal sintering route. Figure 1.2 shows some of the applications of metal foams used in thermal management.

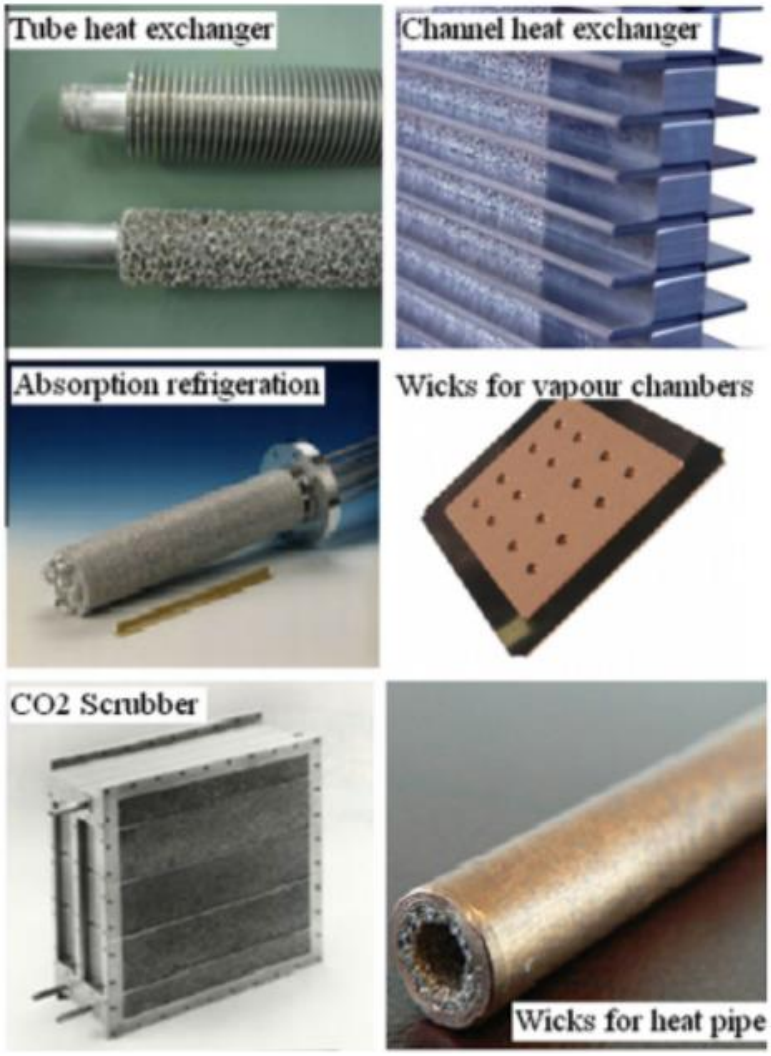

Figure 1.2: Metal foams applications for thermal transport [3]

Metal foams are predominantly used in convection (forced and natural) with a small amount of research in the field of phase change materials. PCMs have low conductivity and metal foams in combination with a PCM play the role of a thermal conductivity enhancer [4]. Forced convection coupled with heat spreading is a common technique employed in cooling of electronic devices. Compound enhancement techniques [5] which combine two or more cooling techniques are employed for the above purpose. The use of air as working fluid has an inherent limitation of a lower heat transfer coefficient which has to be modified by increasing the surface area and/or

modifying the flow structure. In this regard, high porosity thin metal foams are potential candidates for high heat dissipation. Calmidi and Mahajan [6] studied forced convection in metal foams in a channel flow configuration to develop an empirical correlation to determine interstitial heat transfer coefficient and quantifying thermal dispersion. As seen in Figure 1.3, flow through metal foams follows a tortuous path which leads to enhanced flow mixing and greater turbulence contributing to higher heat transfer. The flow path also offers higher pressure drop and hence an optimum configuration must be able to balance the increment in heat transfer without a large penalty in pumping power.

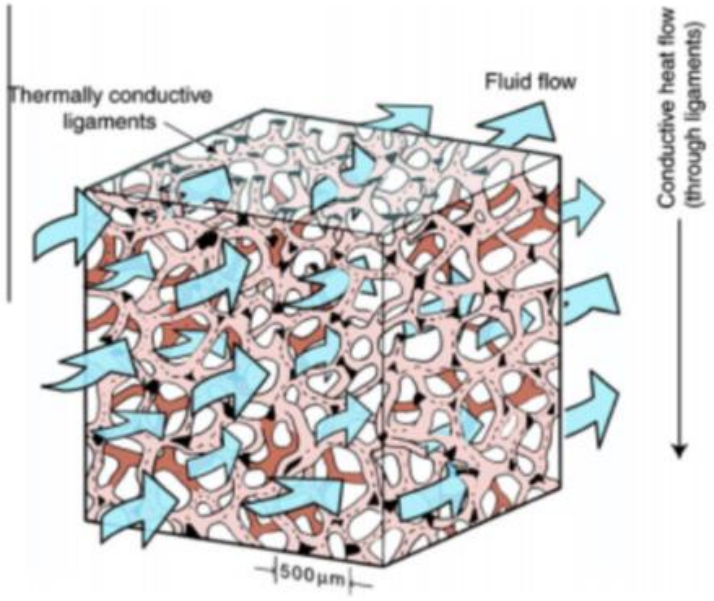

Figure 1.3: Flow through metal foams [3]

A number of experimental and numerical studies were performed for metal foams in channel flow configurations to optimize various parameters like foam porosity, foam pore-density and other geometrical parameters of a channel [7]. Forced convection in the form of jet impingement is a widely used technique for high rate of heat removal from a stagnation zone [8]. Jet impingement involve air impinging orthogonally onto a heated surface and then follow a

constrained exit flow scheme. If the fluid after impinging can exit through all the four directions, it is called minimum crossflow. If air is constrained to exit through either one or two directions, it is termed as maximum and intermediate crossflow respectively. Detailed literature survey is presented in Chapter 2 as relevant.

1.3 Objective of the present work and organization

Most of the earlier works where metal foams are used under jet impingement focused on a small geometry often under minimum crossflow conditions. This limited the experimental studies to pressure and heat transfer data on a global scale. In this study, a long channel is specifically chosen to locally characterize flow and heat transfer to accurately predict where heat transfer enhancement is observed. This geometry also gives the advantage of controlling the exit schemes for jet impingement where intermediate and maximum crossflow schemes are studied for all the foam configurations. 5 different metal foams are used in this study to separately study the effects of foam pore density and foam heights under these crossflow schemes. This work would give thermal designers information about local heat transfer enhancement to effectively choose metal foam cooling configurations to be used in the electronics cooling industry.

Chapter 1 provides general description about different cooling strategies involved in electronic cooling and details the choice of using metal foams in thermal management applications.

Chapter 2 presents the detailed literature survey related to heat transfer studies for jet impingement onto thin metal foams. This is followed by describing the experiment and detailed discussion about the results of the study.

Chapter 3 presents the conclusions of the present work and scope for future studies.

REFERENCES

1. Cengel, A., 2007. HEHT TRANSFER
2. Kraus, A.D. and Bar-Cohen, A., 1983. Thermal analysis and control of electronic equipment. *Washington, DC, Hemisphere Publishing Corp., 1983, 633 p.*
3. Zhao, C.Y., 2012. Review on thermal transport in high porosity cellular metal foams with open cells. International Journal of Heat and Mass Transfer, 55(13-14), pp.3618-3632.
4. Baby, R. and Balaji, C., 2013. Experimental investigations on thermal performance enhancement and effect of orientation on porous matrix filled PCM based heat sink. *International Communications in Heat and Mass Transfer*, *46*, pp.27-30.
5. Bejan, A. and Kraus, A.D., 2003. Heat transfer handbook (Vol. 1). John Wiley & Sons.
6. Calmidi, V.V. and Mahajan, R.L., 2000. Forced convection in high porosity metal foams. Journal of heat transfer, 122(3), pp.557-565
7. Bhattacharya, A. and Mahajan, R.L., 2002. Finned metal foam heat sinks for electronics cooling in forced convection. *J. Electron. Packag.*, *124*(3), pp.155-163.
8. Viskanta, R., 1993. Heat transfer to impinging isothermal gas and flame jets. Experimental thermal and fluid science, 6(2), pp.111-134.

CHAPTER 2

Array jet impingement on high porosity thin metal foams: effect of foam height, pore-density and spent air crossflow scheme on flow distribution and heat transfer

Vivek Subramaniam Sambamurthy 1, Srivatsan Madhavan 1, Prashant Singh 2, Srinath V. Ekkad 1
1 Department of Mechanical and Aerospace Engineering
North Carolina State University, Raleigh NC 27695
2 Department of Mechanical Engineering, Mississippi State University, Starkville MS 39762

2.1 Introduction

As the demand for miniature and high-powered electronics increases, the development of highly efficient cooling concepts is imperative. High porosity metal foams are a popular choice in this regard, as they offer significant enhancement in heat transfer over other cooling concepts [1]. The high heat dissipation offered by metal foams is attributed to the high surface area-to-volume ratio, enhanced flow mixing, thermal dispersion caused by highly tortuous flow paths, and high effective thermal conductivity due to the presence of metallic fibers [2]. Hunt and Tien [3] attributed heat transfer enhancement to non-Darcian effect like thermal dispersion and showed that forced convection in metal foams can be described by a single energy equation to model the transport. Lu et al. [4] developed a numerical model that was based on crossflow across a bank of cylinders to mimic flow through foams. Overall heat transfer coefficients and pressure drop for flow through foams were obtained through an analytical model. Calmidi and Mahajan [5] developed an analytical model for effective thermal conductivity of metal foams, by taking into consideration the unit cell structure. Calmidi and Mahajan [6] also developed a local thermal non-equilibrium (LTNE) model from energy transport from metal fibers to fluid when the temperature difference between the two was appreciable. They concluded that dominant mode of heat transfer was through solid phase conduction, interfacial convection and negligibly affected by dispersion for the air-aluminum combination. Bhattacharya and Mahajan [7] reported an enhancement of 1.5-

2 times for the finned metal foam heat sinks over conventional finned heat sinks. Above numerical studies were based on volume-averaging method. Diani et al. [8] carried out pore-scale simulations and reported that metal foam ligaments acts as obstacles creating tortuous flow path and flow mixing.

The benefits of using metal foams in channel flow has been shown by many other studies apart from the ones listed above. To further enhance the convective transport in metal foams, some studies have used jet impingement onto the foams in different configurations. Jet impingement is typically associated with high heat transfer due to flow stagnation [9-13]. However, when used with metal foams, the flow dynamics is very complicated and has been investigated through many experimental and numerical studies. Kim et al. [14] studied the effects of pore density, jet-to-jet spacing, for aluminum metal foam heat sinks in single-jet and multi-jet impingement system. They reported enhancement of 2-29% with 40 PPI foam yielding maximum heat transfer. Wong [15] determined the temperature distribution on metal foam under jet impingement using infrared thermography and developed a two-dimensional numerical model to benchmark the same. Slot jet impingement onto metal foams has also been investigated extensively [16-21]. A numerical study on confined slot jet impingement on metal foam heat sink was carried out by Jeng et al. [16] and reported heat transfer enhancement levels between 2 to 3 times compared to a configuration without metal foams. The same authors experimentally investigated convective heat transfer and pressure drop in metallic foam with a confined slot jet [17] for various parameters such as the ratio of jet-to-foam top distance to the foam height, the ratio of jet nozzle width to foam height. Their results showed that average Nusselt number decreased with increase in foam height.

Marafie et al. [18] developed a numerical model to study non-darcian effects in slot-jet configuration. They concluded that Nusselt number increased by narrowing the jet-to-heated

surface distance, reducing porosity of the foam and by using a foam that had a higher solid-to-fluid thermal conductivity ratio. Saeid [19] developed a Darcy model for jet impingement on a porous media with initial crossflow and reported that presence of initial crossflow degrades the heat transfer. Buonomo et al. [20] developed an extended Darcy numerical model to simulate slot jet impingement onto a fully filled foam channel invoking the LTNE condition. A significant increase in heat transfer was reported at the end of the heated part due to the presence of metal foam. Saeid et al. [21] studied the effects of different shapes of aluminum metal foams under slot-jet impingement cooling and concluded that convex shaped metal foam heat sink performed the best. Single circular jet impingement onto aluminum metal foams under fixed pumping power condition was experimentally investigated by Byon [22]. Kuang et al. [23] investigated compact copper metal foams heat sinks under axial fan flow impingement. They reported maximum heat transfer for a foam height-to-fan diameter ratio of 0.22 for the ratio of fan-to-heated surface distance and fan diameter of 0.5. Shih et al. [24] determined the optimum height-to-diameter ratio of a cylindrical aluminum metal foam under axial jet impingement. An increasing-decreasing trend was observed in Nusselt number as the ratio was reduced and the optimum value was reported as 0.23. The same research group used a flow mask to partially restrict the spent air radial escape [25]. The Nusselt number improved with increase in the length of the flow restricting mask and a Nusselt number enhancement of 1.2-1.8 times was reported for different heights of the restricting mask. Feng et al. [26] developed a numerical model for finned metal foam heat sinks subject to impinging air cooling and validated the results experimentally. They reported heat transfer augmentation of 1.5-2.8 of finned metal foams over plain metal foam heat sinks. Another study by the same research group was carried out to study the geometrical effects of finned metal foam sinks [27]. They observed that Nusselt number increased with increase in channel length and fin

thickness whereas reduction in Nusselt number was observed with increase in fin height at a given dimensionless developing flow length. A more recent study on finned metal foams [28] by Wang et al. investigated the height effects of finned metal foam under rectangular slot jet impingement and axial fan impingement. They reported that Nusselt number increased with decreasing fin heights and 30 PPI finned metal foam outperformed 20 PPI and 10 PPI for the lowest fin height. Sung et al. [29] studied the effects of a porous mesh in a long narrow channel under jet impingement. They suggested that the porous mesh obstructed the jet flow and reduced the Nusselt number when compared to base case.

Rallabandi et al. [30] evaluated heat transfer enhancement in a rectangular channel for jet impingement under maximum crossflow condition and reported an enhancement of 50-90% for the same. Singh et al. [31] studied array jet impingement onto high porosity thin metal foams at zero jet-to-foam spacing. They reported an increase in heat transfer with increase in pore-density with an enhancement of 2.3-2.8 times the smooth target. A recent study by Madhavan et al. [32] reported a 100% increase in thermal hydraulic performance for array jet impingement onto thin metal foams under minimum crossflow condition and concluded that foams are most efficient when there is no spacing between the jet exit plane and the top part of the foam.

The past studies have shown that jet impingement used in combination with metal foams (especially thin metal foams) provides significant enhancement in heat transfer as well as in thermal hydraulic performance. Some selected studies on jet impingement on metal foams has been listed in Table 2.1 However, array jet impingement in long narrow channels in the presence of metal foams have not yet been explored comprehensively. To our knowledge, there is not significant literature which details local flow and heat transfer distributions in such a configuration.

Therefore, it is necessary to investigate the above configuration and provide complete heat transfer and flow data for the designers.

Table 2.1: Typical Metal foam and Jet Impingement configurations

Configuration	**Ref.**	**Flow Parameters**	**Experimental parameters**	$\boldsymbol{\frac{Nu_{foam}}{Nu_0}}$
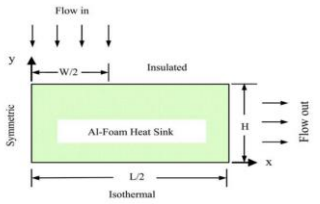	16	$Re = \frac{\rho_f V_j W}{\mu}$ $Re = 100 - 40000$	$\frac{H}{W} = 2,4,6,8$	2-3
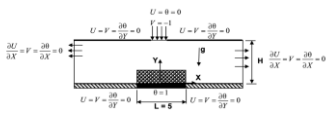	18	$Re = \frac{V_j W_j}{\vartheta}$ $Re = 25 - 400$	$0.01 \leq Ri \leq 1$[1] $10^{-2} \leq Da \leq 10^{-6}$ [2] $0.5 \leq H \leq 4$ $0.25 \leq \varepsilon \leq 1$	2.4
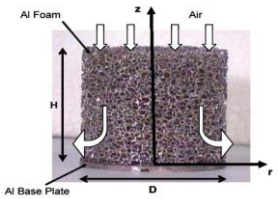	24	$Re_{Dp} = \frac{\rho_f V_j D_p}{\mu_f}$ $Re = 2 - 50$	$0.15 \leq H/D \leq 0.92$ $0.87 \leq \varepsilon \leq 0.96$ $10 \leq PPI \leq 4$	1.2-1.8

[1] $Richardson\ number, Ri = Gr/Re^2$; $Gr\ is\ Grashof\ number$

[2] $Darcy\ number, Da = K/W_{jet}^2$; $K\ is\ permeability\ of\ porous\ medium$

Table 2.1 (continued)

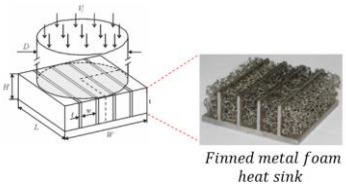 *Finned metal foam heat sink*	26	$Re = \frac{\rho_f V_j D}{\mu_f}$ $Re = 3000 - 14000$	$H = 10 - 40$ $t = 2$ $w = 4$ $L = 68$ $W = 68$ All dimensions in mm	1.5-2.8
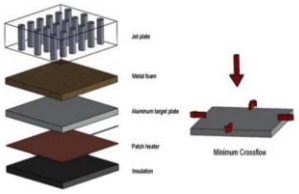	32	$Re = \frac{4\dot{m}_j}{\pi d_j \mu}$ $Re = 3000 - 12000$	$z/d_j = 0.75, 2{,}4$ $x/d_j = 3.42$ $y/d_j = 2$ $\varepsilon = 0.9265$ 40 PPI $50.8mm$ $\times 50.8mm$ $Al\ foa$	1.8-2.5

The present study is focused on a large array of jets where thin metal foams have been used at zero jet-to-foam spacing. Two different crossflow schemes, maximum and intermediate, have also been studied for different foam configurations. Three different foam configurations with pore-densities of 5, 20 and 40 PPI have been studied at a constant foam height of 19.05 mm. To investigate the effect of foam height, three different heights of 3.175 mm (z/d=1), 6.35 mm (z/d=2) and 19.05 mm (z/d=6) for 40 ppi foams have been investigated. In all above configurations, the jet configuration consisting of 10 x 4 jets has been used. The baseline configuration for the foams was

the geometrically identical impingement channel without foam. Following sections provide details of experimental setup, description of test configurations, experimental conditions, followed by discussion of results, and some concluding remarks and recommendations for future studies.

2.2 Experimental setup

A schematic of the experimental setup is shown in Fig. 2.1. Compressed air at 120 psig continuously charged a buffer tank placed in the vicinity of the heat transfer test section such that air supply can be delivered at a constant pressure through the duration of the experiment. Further downstream of the buffer tank, a pressure regulator was installed to reduce the pressure to a required value based on the mass flow rate requirements in the experiments. The laboratory ambient air was allowed to pass through an ASME orifice plate for flow metering. At the orifice plate, the differential pressure between the line and the orifice throat was measured. Further, the static pressure and static temperature of the air was measured and used in conjunction with the differential pressure measured, in an in-house code for mass flow rate calculation. A total entry length of 35 pipe diameters was provided upstream of the orifice plate in order to allow for hydrodynamic flow development. Post the flow metering, the air was routed to the heat transfer test section, which is described in detail in the following section. A similar test facility was used in [32].

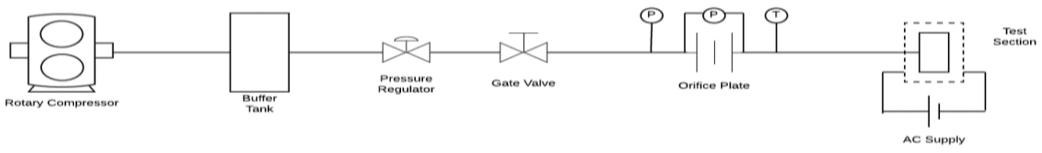

Figure 2.1: Schematic of experimental setup

2.3 Description of test configuration

The heat transfer test section is shown in Fig. 2.2. An array jet impingement was used for convective heat transfer enhancement. The jets were arranged in a 10×4 array such that streamwise jet-to-jet spacing (x/d) was 8, and the spanwise jet-to-jet spacing (y/d) was 4. The jet diameter (d) was 3.175 mm. The jet plate thickness was $4d$, which is typical recommendation to allow the flow development in the jets. Ten aluminum blocks of dimension 50.8 mm by 23.65 mm were placed sequentially separated by spacer insulations to avoid heat transfer between them. Thermocouples holes were drilled right underneath the skin of the target surface and extended till the middle of the block. The thermocouples were connected to a Data Acquisition System (DAQ) for constant monitoring and recording of data. Cartridge heaters connected to a variable AC supply were used to heat the aluminum blocks. They were controlled individually by using ten different power sources. The power input to each aluminum block was calculated by measuring the voltage and resistance across the circuit using a multimeter. The metal foam samples were attached to the surface using a highly conductive thermal paste (Arctic Silver^{TM}) with a reported thermal conductivity of k ~ 8.8 W/mK. Sufficient insulation was provided at the rear side of the target surfaces to minimize heat loss during the experiment. The spent air exit path for an intermediate crossflow scheme has also been shown in Fig. 2.2.

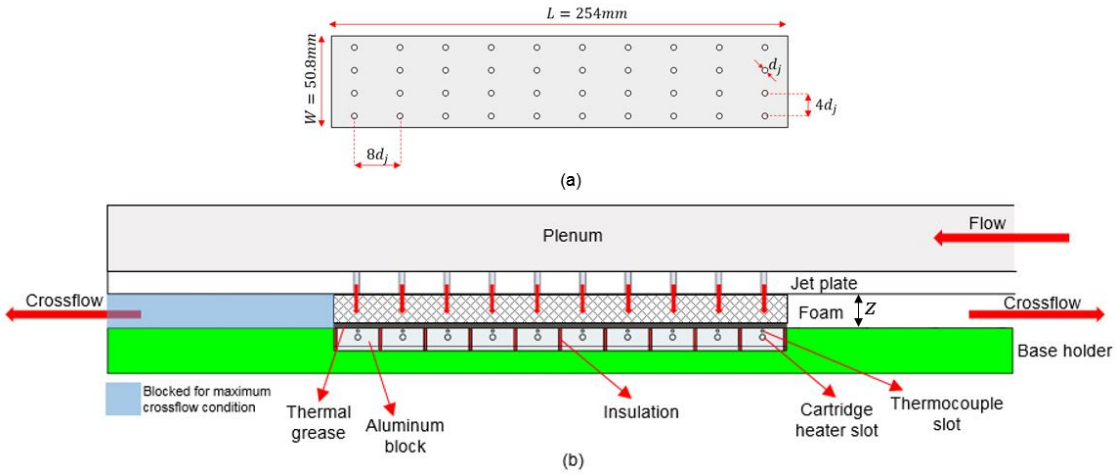

Figure 2.2: (a) details of jet plate (b) details of test section assembly with flow direction.

2.3.1 Details of foam samples

Metal foam samples were made of T6-6101 aluminum alloy with 4-6% relative density and procured from ERG Aerospace. Porosity of the foam samples were measured using a precision weighing balance and was found to be approximately 93% across all pore-densities. Fiber diameter (d_f) was calculated by processing several Scanning electron microscopic images (SEM) images and is provided in Table 2.

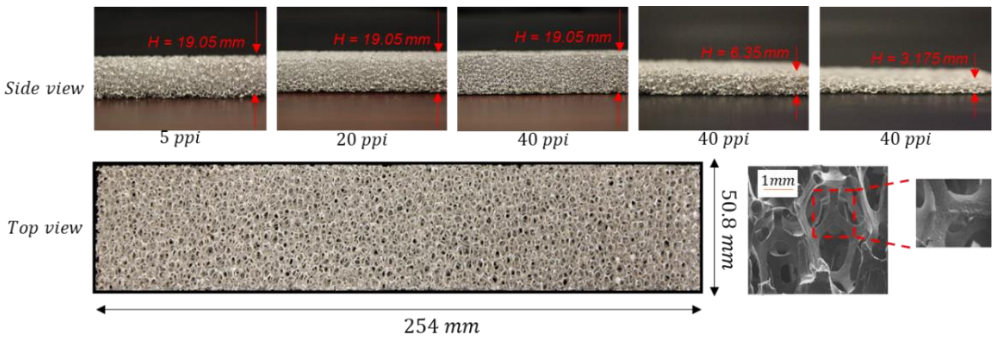

Figure 2.3: Actual photos of foam samples used and SEM image of foam

2.3.2 Determination of permeability (K) and inertial coefficient (C_f)

Using the Forchheimer extended Darcy's equation [33], the pressure gradient across a porous medium is given as:

$$-\frac{dP}{dx} = \frac{\mu u}{K} + \frac{\rho C_f}{\sqrt{K}} u^2 \ (Eq. 1)$$

To evaluate the permeability (K) and inertial coefficient (C_f) from Eq. 1, they need to be simultaneously calculated using two equations. The foams tested in the current study were placed in a channel flow setup and pressure taps were installed across the length of the foam to evaluate the pressure gradient. The thinnest foam sample for each pore-density was tested in these set of experiments. The values for permeability (K) and inertial coefficient (C_f) were obtained and shown in Figure 2.4. The inertial coefficient (C_f) which is a measure of the drag experienced during flow through metal foam fibers, was similar for the three pore-densities. However, permeability (K) reduced with increase in pore-density.

Parameters	5 PPI	20 PPI	40 PPI
PPI	5	20	40
Porosity (ε)	0.9348	0.9309	0.9342
Pore diameter, d_p (mm)	4.34	2.51	2.24
Fiber diameter , d_f (mm)	0.53	0.31	0.27
Specific area, (m^2/m^3)	311.07	1172.98	1685.04
Permeability (K) x 10^7/Inertial coefficient (C_f)	2.61/0.1298	0.862/0.1296	0.7/0.1298

Figure 2.4: Foam properties, permeability and inertial coefficient

2.4 Experimental conditions

A total of 16 different configurations were tested in the current study. Baseline case was impingement onto target surface without the metal foam. The configurations tested are represented in Figure 2.5. Static pressure measurements were carried out in the plenum chamber to evaluate the pumping power. Ten static pressure ports were installed on the target surface to evaluate the local mass flux distribution in the jet array for all cases tested. Experiments were performed for a Reynolds number (Re) range of 3000 – 12000 which corresponds to a mass flow rate of $\sim 5 - 23$ g/s. The temperature of the working fluid was approximately 20 ℃.

Crossflow condition	Configuration	Jet to target distance (z/d)	Pore density (ppi)
Intermediate	Baseline w/o foam	1	NA
		2	
		6	
	With foam	1	40
		2	40
		6	5
			20
			40
Maximum	Baseline w/o foam	1	NA
		2	
		6	
	With foam	1	40
		2	40
		6	5
			20
			40

Figure 2.5: Description of test configurations

2.5 Flow distribution and heat transfer coefficient calculation procedure

2.5.1 Flow distribution calculation

2.5.1.1 Baseline configurations

Discharge coefficient (C_d) is required to determine the flow distribution in jet impingement configurations. In order to calculate the discharge coefficient, the target plate was removed, and jets were allowed to vent into the laboratory ambient, a procedure similar to [11]. Plenum pressure was measured at several locations, and it was found that their values were near-similar to each other, hence ensuring that a constant pressure plenum was feeding the jets. The average of these static pressures was used as the plenum pressure for further calculation. Further, the investigated Reynolds numbers (based on jet diameter) corresponds to jet Mach numbers lower than 0.1, thus allowing the use of incompressible flow equations. The discharge coefficient, C_d is the ratio of the actual mass flux and the ideal mass flux. Since for the above test setup, where the jets were not restricted or were simply allowed to escape into the ambient, it can be assumed that each jet was subjected to uniform mass flux. For above conditions, the discharge coefficient can be given as, $C_d = \dot{m}_{actual,jet}/(0.25\pi d^2\sqrt{2\rho\Delta p}) = (\dot{m}_{actual,total}/N)/(0.25\pi d^2\sqrt{2\rho p_{plenum}})$. Now, the total mass flow rate ($\dot{m}_{actual,total}$) through all the jets was measured by the orifice plate. Through the above procedure, the C_d was found to be 0.76 and a weak dependence on the jet Reynolds number was observed.

For the flow distribution, separate experiments were conducted where the target plate was also assembled onto the jet plate with the help of a spacer sandwiched between the two. A total of 10 pressure taps were machined exactly mid-way between the two adjacent jet centers and in the streamwise direction, to measure the local pressure differential between the constant plenum

supply pressure and the local position in the impingement channel. This procedure is also similar to [11]. Now, with the knowledge of the discharge coefficient and the local differential pressure, the mass flow rate in each row was determined through, $\dot{m}_{row} = N_{jets,row}\dot{m}_{j,row} = N_{jets,row}C_d(0.25\pi d^2\sqrt{2\rho(\Delta p_{row})}$, where $N_{jets,row}$ is the number of jets in a row (=4) and $\dot{m}_{j,row}$ is the mass flow rate through each of the jet in a particular row. Above equation has an implicit assumption that each jet in a particular row receives the same mass flow rate. In this paper, the local mass flow rate is presented in terms of ratio of local jet mass flux $G_{j,row} = (\dot{m}_{row}/N_{jets,row}A_{jet})$ with the average jet mass flux ($\bar{G}_j = \mu\overline{Re_j}/d$), to be consistent with the correlation prescribed by Florschuetz et al. [11] and facilitate the validation. Further, the crossflow mass flux accumulation is calculated based on the row-wise jet mass flux distribution calculated through above procedure, and is given as, $G_{c,i} = \sum_{i=1}^{i=i-1} G_{j,i}\,(A_j/A_c), \forall i \in [2, N_{rows}]\ and\ G_{c,1} = 0$. The crossflow mass flux is presented in a normalized form ($G_{c,i}/G_{j,i}$), where "i" is the row number. For simplicity, the index notation based on "i" is dropped in the later plots. For accuracy check, $(G_{c,10} + G_{j,10})$ was compared with the total mass flux measured by orifice meter and the difference between the two was found to be within 4%, thus supporting the validity of above procedure with implicit assumptions for determination of flow distribution in the impingement channel.

2.5.1.2 Metal foam configurations

The procedure for jet mass flux distribution in metal foam configurations was different from baseline impingement configurations without foams. A different procedure was followed for the foam configurations because the flow was governed by both, incompressible flow in the

nozzles and the Darcy-Forchheimer equations in the metal foam region, as opposed to only incompressible flow equations in the baseline configurations.

The flow distribution experiments for foam configurations were carried out in two stages. Firstly, the method similar to the baseline configuration was followed, with the difference being the impingement channel was occupied by metal foam. The plenum pressure was measured, along with the corresponding static pressures in the impingement channel, corresponding to each jet row. The pressure difference at each jet row was measured. The second stage of experiments involved selective opening of a single row of jet while keeping all other rows blocked. Now, the pressure difference between the plenum chamber and the opened row was set equal to the one found in the previous experiment when all the rows were opened together. Once the desired pressure differential was set, the mass flow rate through that row was measured through the orifice plate calculations. This procedure was repeated for other jet rows as well. The individual mass flow rates thus obtained when added together, was found to be within 5-10% of the total mass flow rate measured in the 1st stage of the flow experiments for foam configurations. This method, however, does not include the crossflow effects on coolant distribution. The above effect can be ignored since a global mass balance was observed between the two different types of experiments. For further testing of the 2nd method proposed for the foam configuration, experiments were carried out on the baseline configuration as well. The total mass flow rates obtained in the method prescribed in section 2.5.1 and above was found to be within ±2%. Considering the above observations, the 2nd method was deemed appropriate for calculating the jet mass flux distribution for foamed configurations.

2.5.2 Heat transfer coefficient calculation

Row-wise averaged heat transfer coefficient was calculated through Eq. 2, where T_w is the local wall temperature of each aluminum block during forced convection experiment and T_{pl} is the static air temperature measured in the plenum chamber. All the aluminum blocks were heated through separate cartridge heaters which allowed temperature control over each one of them. Further, they were insulated from each other such that there are no lateral heat losses between the two adjacent aluminum blocks. The heat flux for each aluminum block was adjusted such that a uniform temperature can be maintained across all ten blocks. Above practice also ensures that the lateral heat losses between two adjacent blocks was negligible. Although the thermal boundary condition is of the type constant heat flux, due to the high thermal diffusivity of aluminum and the block size being rather small, the temperature of the block was also near-uniform.

$$h = \frac{(q"_{total})_i - (q"_{loss})_i}{T_w - T_{pl}} \ (Eq. 2)$$

In order to maintain a constant temperature boundary condition, heat flux input to each aluminum block was varied along the streamwise direction. This is denoted by the running index i which runs from 1 to 10 in the present study. Heat supply $(q")$ is calculated by measuring the voltage and resistance across the circuit using a multimeter. Separate experiments were carried out to quantify the heat loss $(q"_{loss})$. For such experiments, the air supply was cut off and a certain heat input was provided to each aluminum block such that all ten can be maintained at the same temperature T_w. Heat losses in case of foam was found to be higher than their corresponding baseline cases by about 15%. The contribution of heat loss to the total heat flux was found to be about 10% across all foams tested. Note that such a method for calculating convective heat transfer coefficient will yield the true contribution of forced air and is prescribed for studies where thermal

grease is used to attach foams onto a heated base. This procedure eliminates the effect of contact resistance between metal foam and heated base. Heat transfer coefficients obtained through the above procedure is presented in the normalized form given in Eq. 3.

$$Nu = hd/k_f \ (Eq. 3)$$

It should be noted that the characteristic length in the current study is taken as the jet diameter (d) and the thermal conductivity (k_f) is calculated at the film temperature, i.e. the average of wall and fluid temperatures.

2.6 Uncertainty quantification

Uncertainty in Nusselt number was obtained using the sequential perturbation analysis prescribed by Moffat [14]. Error propagation for any property P as a function of n independent variables R is given as:

$$\delta P = \sqrt{\sum_{i=1}^{n} \left(\frac{\partial P}{\partial R_i}\delta R_i\right)^2} \ (Eq. 4)$$

The uncertainty in Nusselt number calculation is due to uncertainty in measurements of area (A_s), temperature (T), voltage (V) and resistance (R). The uncertainty in area measurement was taken to be 2%. The uncertainty in voltage and resistance measurements was taken from the manufacturer's datasheet and was found to be 1% and 0.5%, respectively. The uncertainty in temperature measurements was $\pm 0.5℃$. For a maximum Nusselt number from the current study, the overall uncertainty in Nusselt number calculated from Eq. 4 was found to be 5.55.%. An average uncertainty of 3 – 5% was obtained in the entire range of study.

2.7 Results and discussion

This section presents flow and heat transfer data for all configurations listed in Figure 2.5. Firstly, the flow distribution results for the two crossflow schemes is presented for baseline and foam cases, where separate effects of height and pore-density is discussed. The flow distribution results are followed by the local row-wise averaged Nusselt number distribution for the two crossflow schemes for 40 ppi foams, where the effect of foam height on heat transfer is discussed. Similarly, the pore-density effect is presented for both the crossflow schemes and the results are discussed in reference to a corresponding baseline case of no foam. The section concludes with the globally averaged Nusselt numbers, relative enhancements in heat transfer and variation of heat transfer coefficient with pumping power for different crossflow schemes.

2.7.1 Flow distribution

Figure 2.6 presents the flow distribution plots, where separate effects of foam height and pore-density are presented. The baseline configuration is also shown in every plot through circular markers, and the solid line shows the analytical solution presented by Florschuetz [11]. The baseline configurations agreed well with the Florschuetz correlation. For the intermediate crossflow configurations (Figure 2.6a), due to the symmetric nature of crossflow exit, the flow distribution results are presented only for one-half of the impingement channel, i.e. 5 rows. The effect of foam height was studied for the pore-density of 40 ppi. It is observed that the 40 ppi foams at z/d=1 had significantly larger flow resistance as opposed to the baseline configuration, leading to a highly skewed jet mass flux distribution, with the row closest to the exit receiving ~10 times more coolant than the center row (1^{st} row in Figure 2.6a). With increasing z/d, this flow resistance reduced, and the jet mass flux distribution approached a more uniform trend. For the

thickest foam (40 ppi), the jet mass flux distribution was near-uniform and very close to the baseline configuration.

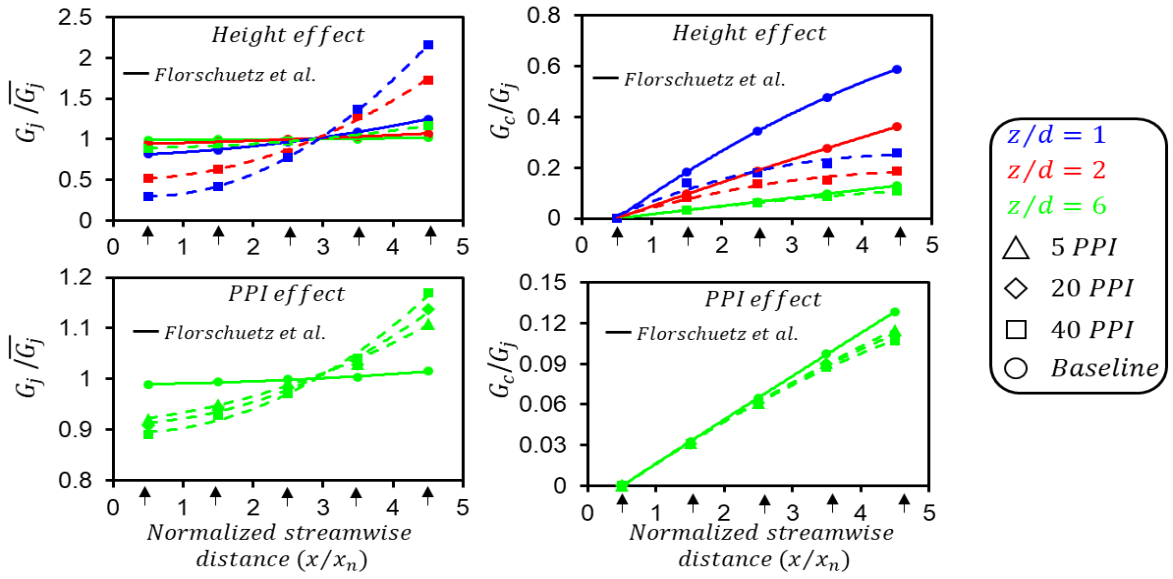

(***a***)

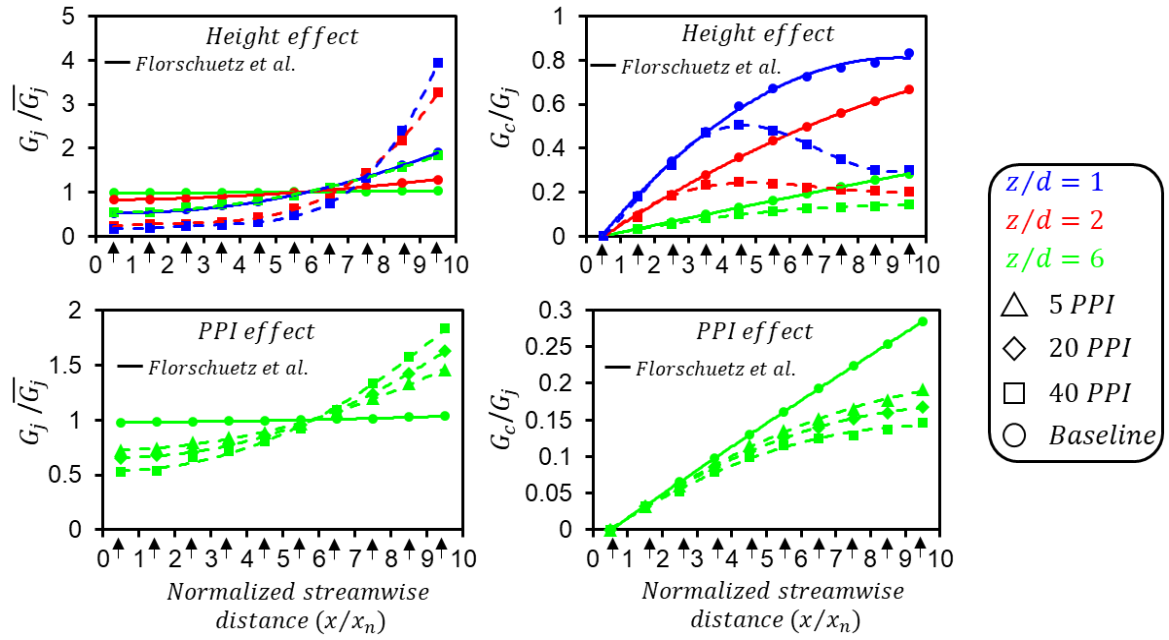

(***b***)

Figure 2.6: Local jet mass flux (G_j) to average jet mass flow ($(\overline{G_j})$) ratio distribution and crossflow mass flux (G_c) to jet mass flux distribution (G_j) ratio distribution for baseline and foam configurations, (a) intermediate crossflow, (b) maximum crossflow

The crossflow mass flux is simply derived from the jet mass flux, and in general shows that the crossflow mass flux strength builds up as the coolant escapes the impingement channel. Due to highly skewed jet mass flux distribution of 40 ppi foams at z/d=1, the crossflow strength at the last row was weak compared to the baseline configuration which had more uniform jet mass flux distribution.

The pore-density effects have been studied for the thickest foam configuration (z/d=6). As expected, due to reduction in flow permeability in increasing pore-density (see Figure 2.4), the flow resistance increases which results in skewed jet mass flux distribution for the larger pore-density configuration. It is noted that all foam configurations received reduced coolant in the center rows and this effect was intensified with the increase in pore-density. The baseline configuration, on the other hand, received more uniform coolant mass flux. As a result, the crossflow mass flux strength for the baseline case increased at a faster rate as compared to any of the three pore-density foams, hence higher degradation in heat transfer is expected for the baseline configuration. This effect will be further discussed in the heat transfer results discussion.

The maximum crossflow scheme configuration results in asymmetrical jet mass flux distribution, and hence is presented for all rows (Figure 2.6b). The flow resistance offered by combined effects of reduced permeability and low jet-to-target spacing resulted in an even more skewed jet mass flux distribution for the 40 ppi foams. For instance, the last row of jets in 40 ppi foams (z/d=1) configuration received ~22 times more jet mass flux compared to the first row. Such an arrangement of jet mass flux distribution results in highly non-uniform distribution of heat transfer and is discussed at a later stage. As a result of above-mentioned geometrical constraints, the resultant crossflow mass flux strength relative to jet mass flux for the z/d=1 40 ppi foams started to reduce post the 5^{th} row. Note that this does not imply the reduction in crossflow mass

flux, which in any case, always increases with increasing streamwise distance from a blocked end. This particular foam configuration (40 ppi, z/d=1) resulted in a unique G_C/G_j distribution, which is atypical of jet impingement heat transfer systems. A slight reduction in G_C/G_j was also observed for the z/d=2 configuration post the 5th row, whereas the z/d=6 configuration had a monotonically increasing G_C/G_j, similar to the baseline configurations. As opposed to the foam configurations, the G_C/G_j for the baseline configuration was always increasing, resulting in higher relative strength of crossflow mass flux in the exit rows. For the pore-density effects, the trends were similar to the intermediate crossflow scheme, with a difference that the jet mass flux was skewed more in the case of maximum crossflow due to increased distance of the blocked end from the zero-gage pressure zone. The skewness extent was inversely proportional to the foam permeability (at fixed z/d=6), which is an expected trend. Above flow redistributions have interesting implications on corresponding heat transfer distributions.

Figure 2.7 gives the variation of supply pressure with Reynold's number. As mentioned earlier, increased resistance leads to increase in Pumping power. It is seen that pressure drop increases with increase in pore-density and decrease in jet-to-target spacing. This supply pressure is later used to calculate the pumping power requirements to maintain the Reynold's number. The increment in supply pressure is the penalty paid to obtain the heat transfer enhancement which drives us to optimize the foam configurations under consideration. It is also significant to note the increase in supply pressure values for maximum crossflow over the intermediate crossflow conditions at a given Reynold's number for a particular foam.

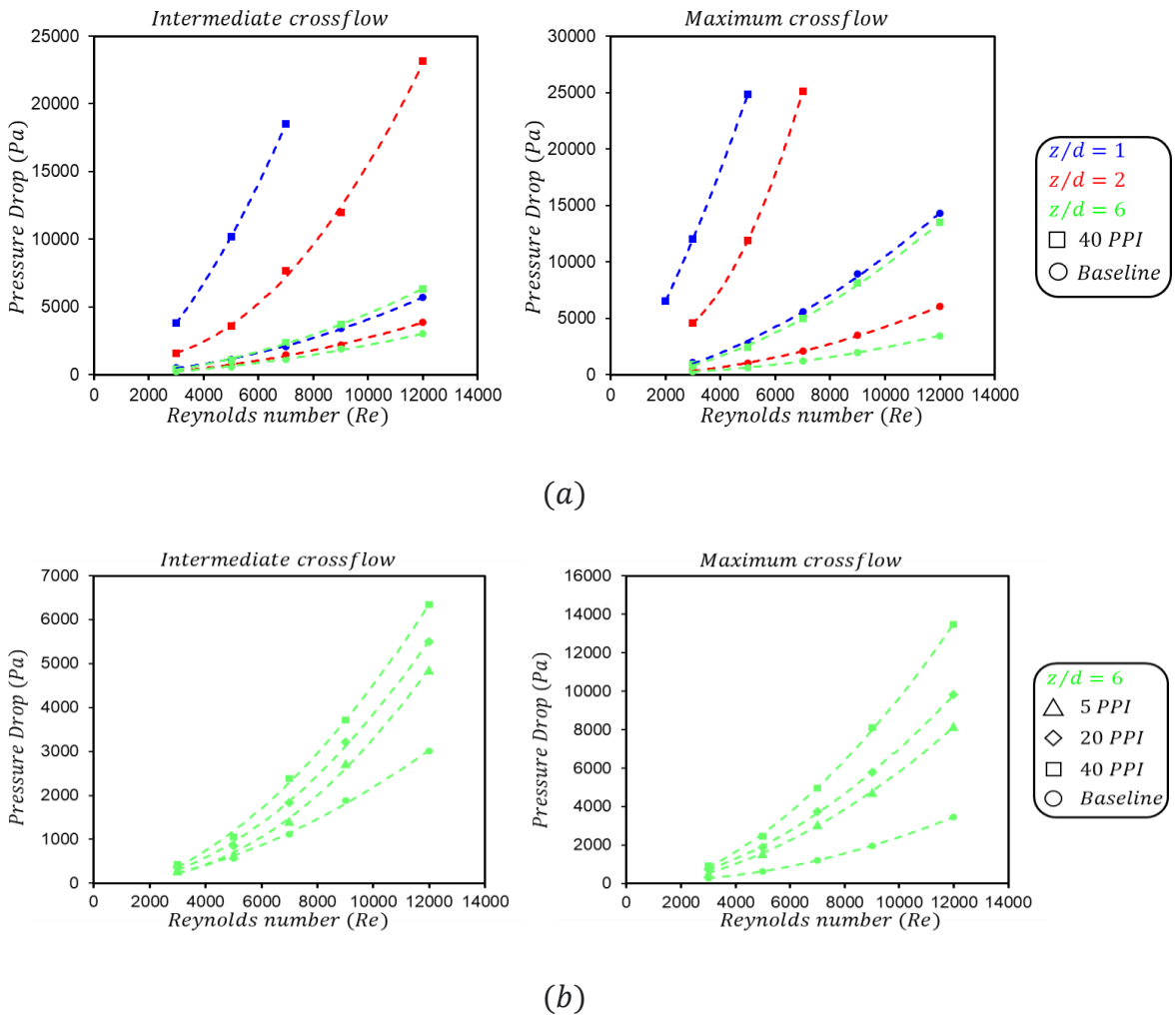

Figure 2.7: Variation of supply pressure drop with Reynold's Number for (a) Height effect (b) PPI effect under intermediate and maximum crossflow conditions

2.7.2 Row-wise Nusselt number distribution

2.7.2.1 Baseline heat transfer and validation with Florschuetz et al. [11]

The row-wise averaged Nusselt numbers for the intermediate and maximum crossflow schemes for baseline configuration (without foam) is presented in Figure 2.8. The experimental data has been shown through filled markers and the trendline obtained from the Florschuetz correlation is shown by solid lines. The validation has been shown for the prescribed z/d's of 1

and 2. Similar to the flow distribution validation, the local Nusselt numbers obtained experimentally agree well with the correlation.

For the intermediate crossflow scheme (Figure 2.8a), the vertical dashed line represents the channel center from where the crossflow accumulation starts. A near-symmetry in heat transfer distribution has been observed along the impingement channel centerline for all jet-to-target spacings. The rows near the centerline had high heat transfer due to absence of crossflow, although they also received lower coolant mass flux compared to other rows towards the impingement channel exit. With increasing streamwise distance from the channel centerline, the jet mass flux increases (Figure 2.6a) along with the crossflow mass flux, leading to an interplay between the two, as the former directly results in higher Nusselt number due to enhanced stagnation heat transfer, whereas the latter results in jet deflection and hence degradation in jet impingement effectiveness. For the lowest jet-to-target spacing (z/d=1), a steady decrease in heat transfer was observed due to accumulation of crossflow leading to jet deflection. However, at this z/d, the last row had higher heat transfer, although being subjected to strong crossflow mass flux.

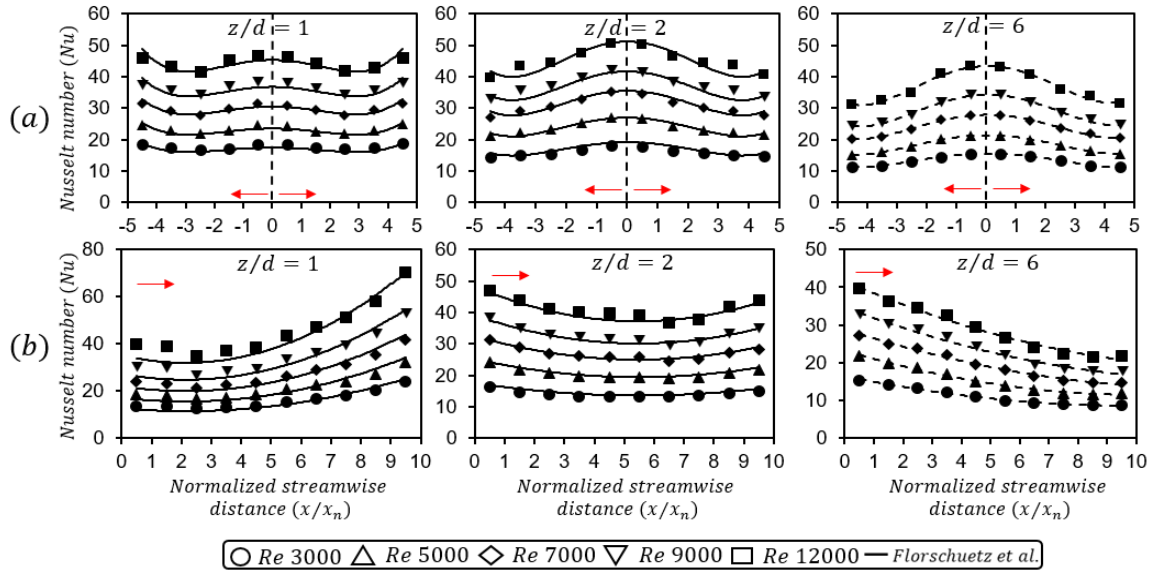

Figure 2.8: Row-wise Nusselt number distribution in baseline configuration for (a) intermediate crossflow, (b) maximum crossflow. Crossflow direction indicated by red arrows.

The two other investigated z/d's (2 and 6) had similar heat transfer distributions for the intermediate crossflow scheme. A near-symmetric and monotonically decreasing heat transfer was observed about the channel centerline, indicating that the crossflow mass flux strength dominates as the flow moves along the channel centerline and results in jet deflection leading to reduced impingement heat transfer. Once again, the agreement with Florschuetz correlation was reasonable for z/d=2. This is due to the strong jet mass flux distribution skewness towards the last row (Fig. 2.4a), which suppresses the negative effects of crossflow. This increase is also marked by the correlation as well. The comparison with correlation for z/d=6 has not been presented, since it lies outside the prescribed limit of the Florschuetz correlation [11].

Consider the maximum crossflow condition for the baseline configuration (Figure. 2.8b). For the lowest jet-to-target spacing (z/d=1), a slightly different heat transfer trend is observed, where the heat transfer increased monotonically with increasing streamwise distance from the blocked end. The major contributing factor to this trend is a highly non-uniform jet mass flux distribution, where the last row (closest to exit) received ~3.5 times more coolant mass compared to the first row (closest to the blocked end). Through a scale analysis for stagnation heat transfer for a single jet (absence of crossflow), one can show that $Nu{\sim}Re_j^{0.53} \equiv G_j^{0.53}$ [34], which indicates that stagnation heat transfer ratio between the last row (#10) and the first row (#1), $Nu_{10,stag}/Nu_{1,stag} \sim \left(G_{j,10}/G_{j,1}\right)^{0.53} = 1.95$ ($Re{\sim}12{,}000$). The row-wise averaged Nusselt number ratio between the last and the first row, $Nu_{10,row-wise}/Nu_{1,row-wise} \sim 1.77$, which again indicates that there was an interplay between the jet mass flux distribution and the crossflow mass flux. This increasing trend in heat transfer with increasing streamwise location from the blocked end in the maximum crossflow condition for low jet-to-target spacings (z/d~1) is also observed in Li et al. [12] and Singh and Ekkad [35]. The local heat transfer trends for the intermediate jet-to-

target spacing (z/d=2) for maximum crossflow scheme was different from z/d=1, due to differences in flow distribution and hence the crossflow mass flux distribution. A slight increase was observed in the last two rows (closer to exit) as the high jet mass flux suppressed the detrimental effects of crossflow. This trend is also shown to have an excellent agreement with the Florschuetz correlation [11]. For the largest jet-to-target spacing (z/d=6), a monotonically decreasing trend is observed, which is expected. A comparison of above-mentioned baseline configurations at a global scale is presented at a later stage.

2.7.2.2 Jet impingement heat transfer in metal foam configurations

This section presents the heat transfer characteristics of jet impingement in a channel packed with metal foams. Forced convection through metal foams results in high rates of heat dissipation due to the increased heat transfer participation area, enhanced mixing due to flow through highly tortuous flow paths and in some fluids (e.g. water), due to enhanced thermal dispersion. In present study, the MF configurations were developed to achieve high foam participation area and to enhance the local flow velocities at fiber and pore levels to enhance the interstitial heat transfer coefficient, by employing thin foams and using array of jets, respectively.

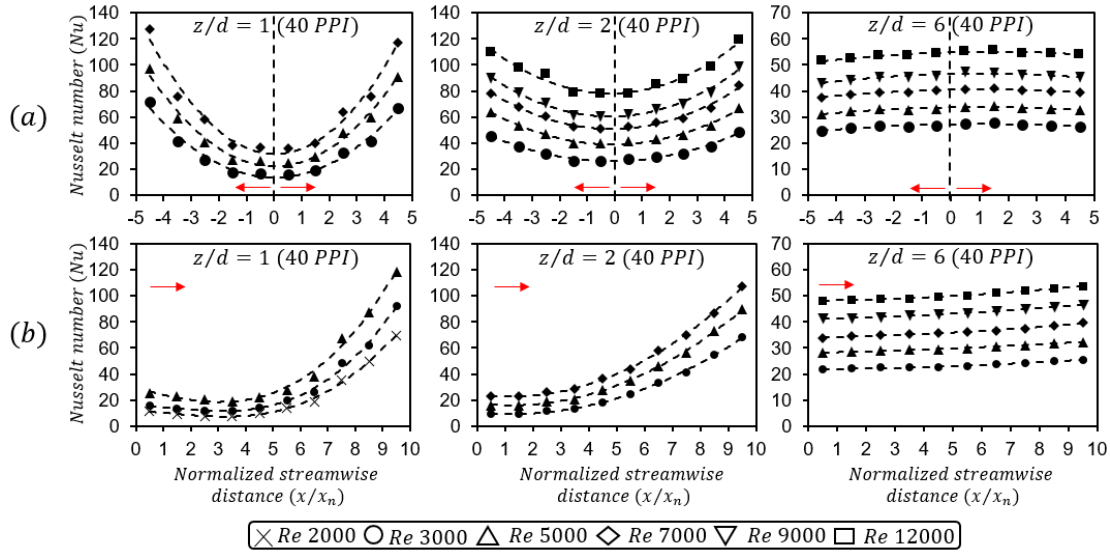

Figure 2.9: Row-wise Nusselt number distribution in 40 ppi foams for (a) intermediate crossflow scheme, (b) maximum crossflow scheme (effect of foam height for a fixed pore-density). Crossflow direction indicated by red arrows. Effect of foam height at fixed pore-density.

To this end, for a fixed pore density (40 ppi), different foam heights of z/d = 1, 2 and 6 were investigated (Figure 2.9), and for a given height of z/d = 6, three different pore densities of 5, 20 and 40 ppi were investigated (Figure 2.10), to study the effects of MF thickness and pore-densities individually. Figure 2.9a shows the row-wise averaged Nusselt Number distribution for 40 PPI MF at different z/d = 1,2 and 6 subjected to intermediate crossflow scheme. It is observed that the Nusselt number distribution is symmetrical about the central row of jets for all the foam thicknesses. The heat transfer distribution trends were significantly different for each foam thickness in comparison with one another, and when compared to respective baseline configurations. The heat transfer was observed to increase monotonically, about the centerline, along the streamwise direction for the two thinner foams, while the heat transfer marginally reduced with increasing streamwise distance for the thickest foam case. In this study, uniformity in heat transfer distribution is defined as the ratio of difference between the highest and lowest

Nusselt number to the average Nusselt Number. $\frac{Nu_{highest}-Nu_{lowest}}{Nu_{average}}$. The uniformity factor for z/d=1, 2 and 6 was calculated to be 1.5, 0.6, 0.1, respectively. The above observations can be explained by the flow distribution results that was discussed in section 7.1. Consider the z/d=1 case, the flow distribution results indicate that the end rows received ~ 10 times more mass flux compared to row at the center of impingement channel. From Figure 2.6(a), it is also seen that G_c/G_j is lower compared to the baseline case, hence the effect of crossflow is not as pronounced. This results in significant increase in heat transfer along the streamwise direction for the thinnest foam case.

Figure 2.9(b) presents the same set of results under maximum crossflow exit conditions. For the thinnest foam, a decreasing-increasing trend was observed with increasing streamwise distance from the blocked end, with the lowest heat transfer observed near the center of the system. From the flow distribution, it is observed that the $G_j/\overline{G_j}$ was nearly constant for the first four plates, followed by a sharp increase as the crossflow escapes the impingement channel. For instance, $G_{j,5}/G_{j,1}$ ~1.9, whereas jet mass flux ratio for the first four rows was between 1.1 and 1.3. Recall that the crossflow mass flux continues to increase in this region (first four rows) despite not much change in jet mass flux, resulting in reducing heat transfer. Post the 4th row, the increased jet mass flux strength results in higher heat transfer.

The 2nd jet-to-target configuration (z/d=2) had a monotonically increasing trend in heat transfer along the streamwise distance, indicating that the jet mass flux distribution effect was more dominant as compared to the z/d=1 configuration. The uniformity factor is 2.7, 1.75 and 0.16 for z/d=1, 2 and 6 respectively, which is much more non-uniform heat transfer distribution compared to the intermediate crossflow scheme. A cooling designer can carefully choose either of the two exit schemes depending upon the heat load the target surface is subjected to.

The effect of relative reduction in the strength of crossflow mass flux (G_c/G_j) can be clearly seen in the z/d=6 case. Despite both crossflows yielding a uniform trend, it is important to note that the Nusselt number increases with increasing streamwise distance in maximum crossflow condition while it decreases along streamwise direction in the intermediate crossflow condition. The relative decrease in the strength of crossflow mass flux compared to baseline case completely reverses the trend.

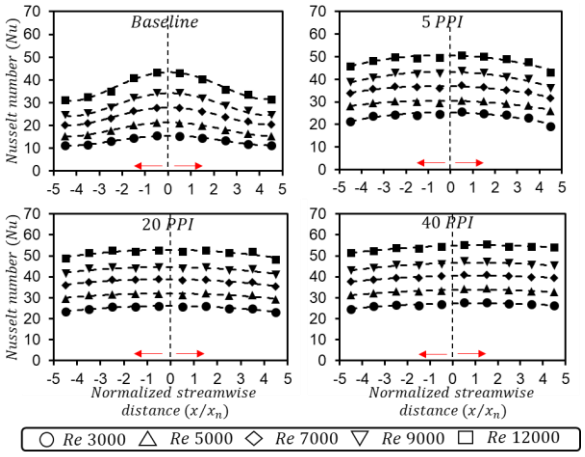

($\boldsymbol{a}$)

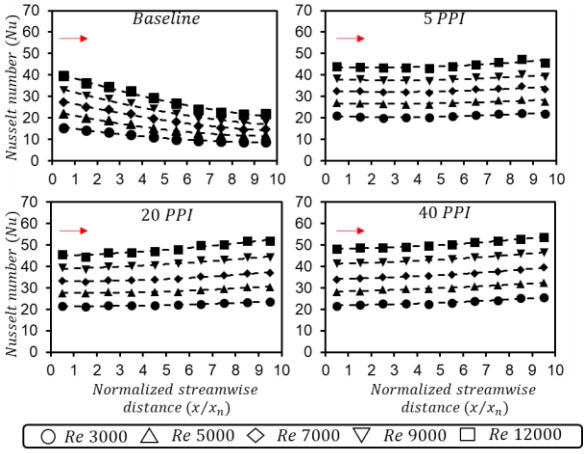

($\boldsymbol{b}$)

Figure 2.10: Row-wise Nusselt number distribution in z/d=6 foams for (a) intermediate crossflow scheme, (b) maximum crossflow scheme (effect of foam pore density for a fixed foam height). Crossflow direction indicated by red arrows. Effect of foam height at fixed pore-density.

Three Pore densities (5 PPI, 20 PPI, 40PPI) are studied at a fixed foam height corresponding to z/d=6, for both intermediate crossflow and maximum crossflow conditions. Figure 2.10(a) presents the results for the various foam pore densities under intermediate crossflow. As expected, the Nusselt number distribution was near-symmetrical along the centerline. Local Nusselt number reduced with streamwise distance for all the three pore densities. Heat transfer distribution was more uniform for higher pore densities while the baseline configuration (without foam) had the maximum non-uniformity. The massflux distribution was similar to that of the baseline configuration because of which heat transfer trends are similar. The crossflow mass flux dominates the jet mass flux distribution and decreases the heat transfer along the streamwise distance.

Under maximum crossflow condition, as shown in Figure 2.10(b), the effect of pore density becomes evident as the trends have minor differences compared to one another. For the 5 PPI foam, the Nusselt number reduced until the 6^{th} row, after which a slight increase was observed. For the 20 and 40 PPI foams, a monotonically increasing trend in heat transfer was observed, from the blocked end. The Nusselt number trends is suggestive of an interplay between the jet mass flux and the crossflow mass flux. As seen in Fig. 2.4(b), the strength of crossflow mass flux reduces with increase in pore-density and this is reflected in row-wise averaged heat transfer distribution. This balance between the two opposing effects on heat transfer results in uniformity associated with the three pore densities tested at z/d=6. It is however interesting to note that most uniform case was the 40PPI foam under intermediate crossflow and 5 PPI foam under maximum crossflow.

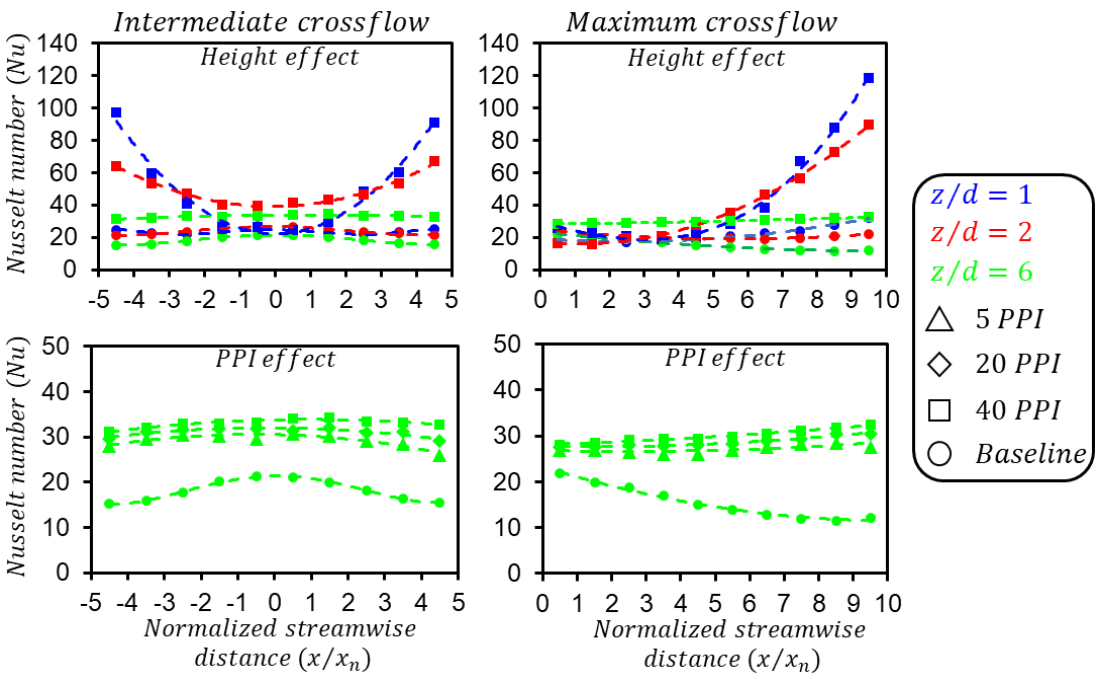

Figure 2.11: Nusselt number variation along the stream wise distance for all configurations at Re 5000

Figure 2.11 gives a summary of the above-mentioned discussion by combining heat transfer data for all configurations at Re=5000. It is observed that maximum enhancement is obtained towards the end of the channel in both the intermediate and maximum crossflow exit schemes. It is seen that in the lowest jet-to-target spacing, some rows receive significantly lower coolant that leads to lower heat transfer than the corresponding baseline case. The thickest foam provides heat transfer enhancement across all the rows leading to a very uniform heat transfer distribution.

2.7.3 Global Nusselt Number variation and Nusselt Number enhancement

This section presents the globally averaged Nusselt number variation with Reynolds number. Heat transfer enhancement is defined as Nu/Nu_0 where Nu is the average Nusselt

number of the metal foam and Nu_0 is the average Nusselt number of the corresponding baseline configuration.

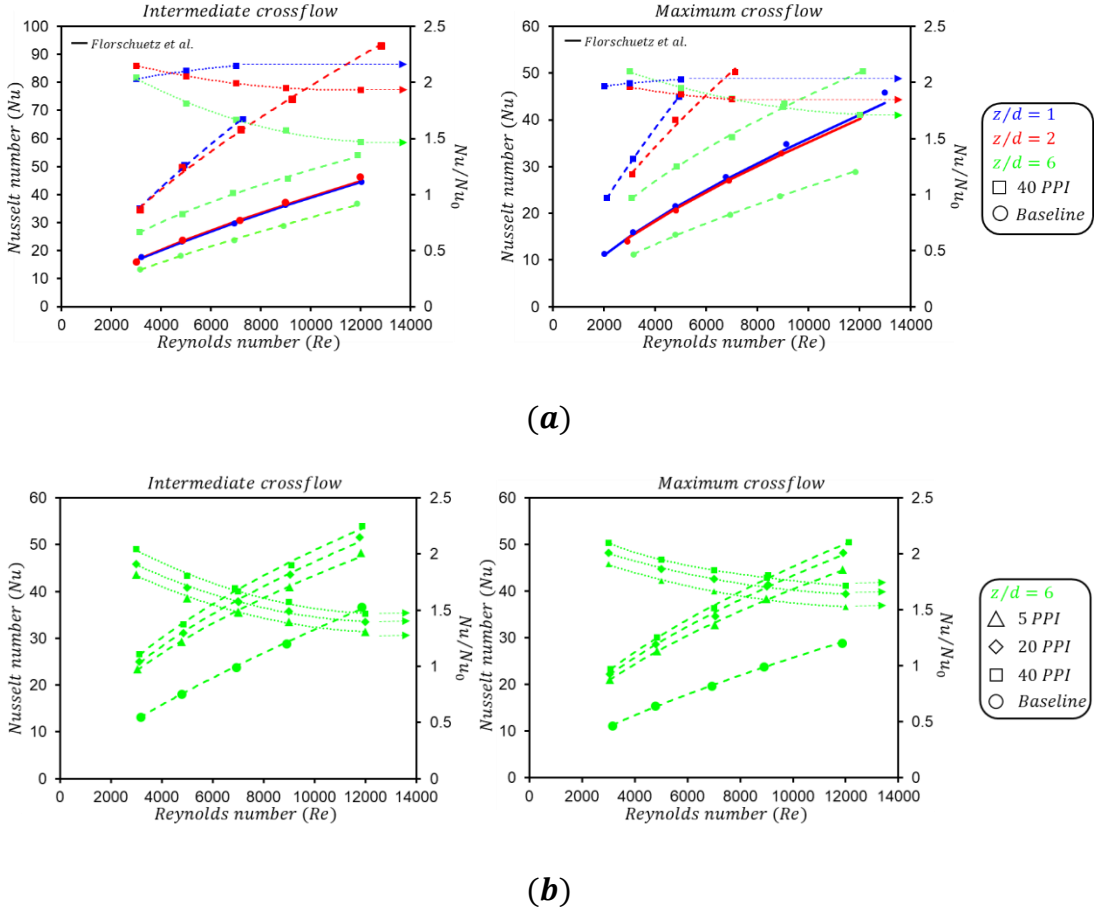

Figure 2.12: Variation of global Nusselt number (primary axis) and Nusselt number Enhancement with Reynolds Number for (a) effect of foam height (b) effect of foam pore densities for intermediate and maximum crossflow conditions

Figure 2.12 (a) presents the foam height effects on global Nusselt numbers. For the global scale as well, the baseline configurations' heat transfer were in reasonable agreement with the Florschuetz correlation [11]. Lower jet-to-target spacing resulted in higher heat transfer for all baseline and metal foam configurations. The heat transfer levels for the two lower jet-to-target spacing were nearly similar and is attributed to relative arrangement of the jets ($(x/d)/(y/d) = 2$ in the current study). Florscheutz et al. [11] reported that the sensitivity of

Nusselt number to z/d increases with jet plate aspect ratio. For example, the effect of jet-to-target spacing was more pronounced for $(x/d)/(y/d) = 3.75$ compared to $(x/d)/(y/d) = 1$. The reduction in heat transfer with increasing jet-to-target distance is attributed to the reduction in the jet potential core strength and some other factors. For further details, the reader is referred to [9]. The heat transfer enhancement shows similar trend for both intermediate and maximum crossflow. The enhancement is maximum at the lowest jet-to-target spacing while it is lowest for the thickest foam.

The heat transfer enhancement mechanism for metal foams is attributed to breaking of high velocity jets into small pockets and their subsequent interaction with the foam fibers. Metal foam fibers can be considered a cylinder and analogies can be drawn from our understanding of flow physics of cylinder in a crossflow. Incoming crossflow impinges onto the cylindrical fibers resulting in enhanced heat transfer due to flow stagnation. Further, the downstream fibers in the wake of the upstream ones interact with small length scale eddies shed, which is also one mechanism which enhances heat transfer.

Figure 2.12(b) demonstrates the pore-density effects on heat transfer. Maximum heat transfer was observed for the highest pore-density (40 PPI), where the enhancement levels varied between 50-100% compared to the baseline configuration. The specific area (surface area-to-volume ratio) increases with increase in pore-density ($311\, m^2/m^3$ for 5 PPI and $1685\, m^2/m^3$ for 40 PPI), signifying higher metal content for 40 PPI foams and hence higher area participating in heat dissipation and highly tortuous flow path which results in enhanced heat transfer. Further, the thermal dispersion effects are also stronger for higher pore-density foams, however with air as the working fluid, this effect is not very significant in this study. Thus, it can be concluded that

the effect of jet-to-target spacing has a more pronounced effect on heat transfer in metal foams as compared to the effect of pore density where thickness of the foam remains a constant.

2.7.4 Heat Transfer Coefficient vs Pumping Power

Above configurations involving metal foams yielded in significant enhancement in heat transfer when compared to the baseline configuration, which itself is considered an effective concept for heat dissipation. However, the gain in heat transfer comes at a cost of increased pumping power in order to maintain the same flow conditions as the one in baseline configuration. Configurations with metal foams had higher flow resistance due to the presence of fibers. Other factors which dictate pressure drop are jet-to-jet spacing, jet-to-target spacing, crossflow exit scheme. Globally averaged heat transfer coefficient has been plotted with respect to associated pumping power for all the configurations in Figure 2.13.

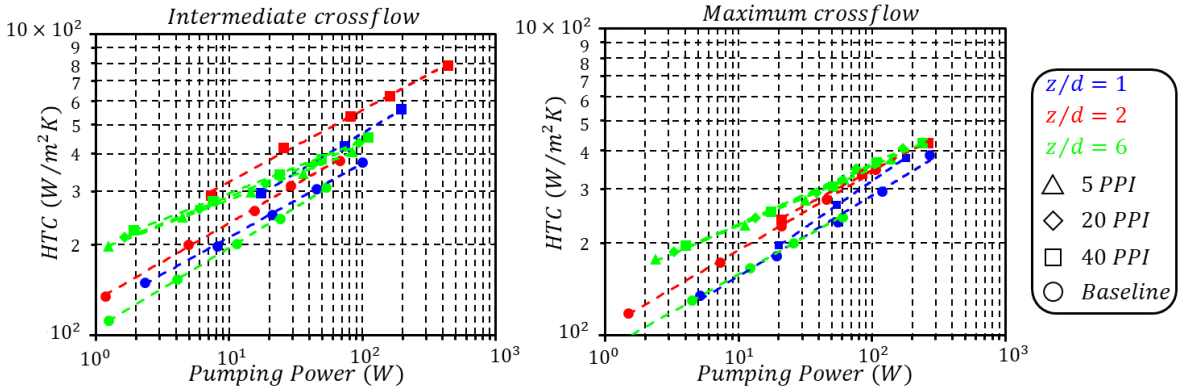

Figure 2.13: Variation of global Heat transfer coefficient with Pumping power (Watts: W) for (a) intermediate crossflow (b) maximum crossflow

All the foam configurations were better in terms of thermal hydraulic performance compared to the baseline configuration. While the jet-to-target spacings of 1 and 2 had near-similar heat transfer levels, the associated pressure losses due to target being closer to the jet exit imposed greater penalty on pumping power, making z/d=2 configurations most effective, when combined

with the intermediate crossflow scheme. However, under maximum crossflow condition, the thickest foam configuration with highest pore-density was the most efficient.

At a constant pumping power of 20W for intermediate crossflow scheme, ~35% increment in HTC is obtained for z/d=2 and z/d=6 cases and ~ 20% increment in the thinnest foam case as compared to their corresponding baseline configurations. Similarly, at a constant pumping power of 100W, the best performing configuration in the intermediate crossflow scheme ($z/d = 2, 40\ ppi$) outperforms the best performing configuration in the maximum crossflow scheme ($z/d = 6, 40\ ppi$) by about 50%.

2.7.5 Correlation for impingement heat transfer

The jet impingement heat transfer for metal foam configurations is summarized in the form of Nusselt number correlations (Eq. 5) and the subsequent coefficients are presented in Tables 2.2 and 2.3 for maximum and intermediate crossflow conditions, respectively. This form of presenting Nusselt number is based on [11].

$$Nu = ARe_j^m \left(1 - B\left[\left(\frac{z}{d}\right)\left(\frac{G_c}{G_j}\right)\right]^n\right) Pr^{1/3} \quad (Eq. 5)$$

Table 2.2: Correlation coefficients (Eq. 5) for maximum crossflow

Configuration	A	m	B	n
z/d=1, 40 PPI	0.341	0.641	0.55	0.527
z/d=2, 40 PPI	0.255	0.601	-0.963	1.917
z/d=6, 40 PPI	0.384	0.561	0.588	2.334
z/d=6,20 PPI	0.291	0.575	0.31	2.615
z/d=6, 5 PPI	0.318	0.555	0.214	1.833

Table 2.3: Correlation coefficients (Eq. 5) for intermediate crossflow

Configuration	A	m	B	n
z/d=1, 40 PPI	0.138	0.723	0.171	0.369
z/d=2, 40 PPI	0.296	0.646	0.923	1.128
z/d=6, 40 PPI	0.443	0.532	0.369	1.908
z/d=6,20 PPI	0.337	0.553	0.624	3.234
z/d=6, 5 PPI	0.359	0.544	0.487	2.001

The correlation predicted Nusselt numbers are compared with the experimentally obtained data, from where the coefficients were determined, in Figure 2.14. Some of the statistics of the above effort are as follows: (a) for maximum crossflow, 92.8% of the total data points (210) lie within the $\pm 15\%$ band (highlighted by black dashed lines), where the points lying outside this band correspond to the two lower jet-to-target spacings, (b) for intermediate crossflow, all the 230 data points lie within the $\pm 15\%$ band (highlighted by black dashed lines).

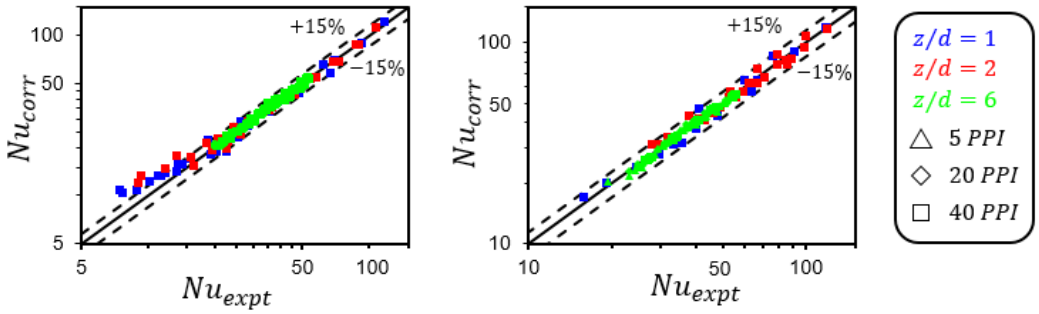

Figure 2.14: Comparison of Nusselt number predicted from developed correlation with the experimental data, for (a) maximum crossflow (b) intermediate crossflow conditions.

NOMENCLATURE

d jet diameter

d_f fiber diameter

d_p pore diameter

A_c Channel cross sectional area

A_j Jet hole cross sectional area

h heat transfer coefficient

k thermal conductivity

K permeability

C_f inertial coefficient

m_j mass flow rate per jet

Nu local Nusselt number

Δp pressure drop across test section

$q"$ heat flux

Re_j jet Reynold's Number ($G_j d_j/\mu$)

G_j jet mass velocity based on jet hole area

G_c channel crossflow mass velocity-based channel cross sectional area

C_d discharge Coefficient

T_{pl} plenum temperature

T_w wall temperature

x streamwise hole spacing

y spanwise hole spacing

z channel height

N total number of jets, 40

Greek symbols

ϵ porosity

ρ density of air

ν kinematic viscosity of air

Superscripts

$(\bar{})$ overbar refers to average value

Subscripts

f fluid

eff effective

REFERENCES

1. Sathe, S. and Sammakia, B., 1998. A review of recent developments in some practical aspects of air-cooled electronic packages. Journal of heat transfer, 120(4), pp.830-839.
2. Zhao, C.Y., 2012. Review on thermal transport in high porosity cellular metal foams with open cells. International Journal of Heat and Mass Transfer, 55(13-14), pp.3618-3632.
3. Hunt, M.L. and Tien, C.L., 1988. Effects of thermal dispersion on forced convection in fibrous media. International Journal of Heat and Mass Transfer, 31(2), pp.301-309.
4. Lu, T.J., Stone, H.A. and Ashby, M.F., 1998. Heat transfer in open-cell metal foams. Acta materialia, 46(10), pp.3619-3635.
5. Calmidi, V.V. and Mahajan, R.L., 1999. The effective thermal conductivity of high porosity fibrous metal foams. Journal of Heat Transfer, 121(2).
6. Calmidi, V.V. and Mahajan, R.L., 2000. Forced convection in high porosity metal foams. Journal of heat transfer, 122(3), pp.557-565.
7. Bhattacharya, A. and Mahajan, R.L., 2002. Finned metal foam heat sinks for electronics cooling in forced convection. Transactions-American Society of Mechanical Engineers Journal of Electronic Packaging, 124(3), pp.155-163.
8. Diani, A., Bodla, K.K., Rossetto, L. and Garimella, S.V., 2015. Numerical investigation of pressure drop and heat transfer through reconstructed metal foams and comparison against experiments. International Journal of Heat and Mass Transfer, 88, pp.508-515.
9. Viskanta, R., 1993. Heat transfer to impinging isothermal gas and flame jets. Experimental thermal and fluid science, 6(2), pp.111-134.

10. Obot, N.T. and Trabold, T.A., 1987. Impingement heat transfer within arrays of circular jets: Part 1—Effects of minimum, intermediate, and complete crossflow for small and large spacings. Journal of Heat transfer, 109(4), pp.872-879.
11. Florschuetz, L.W., Truman, C.R. and Metzger, D.E., 1981, March. Streamwise flow and heat transfer distributions for jet array impingement with crossflow. In ASME 1981 International Gas Turbine Conference and Products Show (pp. V003T09A005-V003T09A005). American Society of Mechanical Engineers.
12. Li, W., Li, X., Yang, L., Ren, J., Jiang, H. and Ligrani, P., 2017. Effect of Reynolds Number, Hole Patterns, and Hole Inclination on Cooling Performance of an Impinging Jet Array—Part I: Convective Heat Transfer Results and Optimization. Journal of Turbomachinery, 139(4), p.041002.
13. Ji, Y., Singh, P., Ekkad, S.V. and Zang, S., 2017. Effect of crossflow regulation by varying jet diameters in streamwise direction on jet impingement heat transfer under maximum crossflow condition. Numerical Heat Transfer, Part A: Applications, 72(8), pp.579-599.
14. Kim, S.Y., Lee, M.H. and Lee, K.S., 2005. Heat removal by aluminum-foam heat sinks in a multi-air jet impingement. IEEE Transactions on components and packaging technologies, 28(1), pp.142-148.
15. Wong, K.C., 2012. Thermal analysis of a metal foam subject to jet impingement. International Communications in Heat and Mass Transfer, 39(7), pp.960-965.
16. Jeng, T.M. and Tzeng, S.C., 2005. Numerical study of confined slot jet impinging on porous metallic foam heat sink. International Journal of Heat and Mass Transfer, 48(23-24), pp.4685-4694.

17. Jeng, T.M. and Tzeng, S.C., 2007. Experimental study of forced convection in metallic porous block subject to a confined slot jet. International Journal of Thermal Sciences, 46(12), pp.1242-1250.
18. Marafie, A., Khanafer, K., Al-Azmi, B. and Vafai, K., 2008. Non-Darcian effects on the mixed convection heat transfer in a metallic porous block with a confined slot jet. Numerical Heat Transfer, Part A: Applications, 54(7), pp.665-685.
19. Saeid, N.H., 2007. Jet impingement interaction with cross flow in horizontal porous layer under thermal non-equilibrium conditions. International Journal of Heat and Mass Transfer, 50(21-22), pp.4265-4274.
20. Buonomo, B., Lauriat, G., Manca, O. and Nardini, S., 2016. Numerical investigation on laminar slot-jet impinging in a confined porous medium in local thermal non-equilibrium. International Journal of Heat and Mass Transfer, 98, pp.484-492.
21. Saeid, Nawaf & Hasan, Nurul & Hairol Bin Hj Mohd. Ali, Mohamed. (2018). Effect of the metallic foam heat sink shape on the mixed convection jet impingement cooling of a horizontal surface. Journal of Porous Media. 21. 295-309. 10.1615/JPorMedia.v21.i4.10.
22. Byon, C., 2015. Heat transfer characteristics of aluminum foam heat sinks subject to an impinging jet under fixed pumping power. International Journal of Heat and Mass Transfer, 84, pp.1056-1060.
23. Kuang, J.J., Kim, T., Xu, M.L. and Lu, T.J., 2012. Ultralightweight compact heat sinks with metal foams under axial fan flow impingement. Heat Transfer Engineering, 33(7), pp.642-650.
24. Shih, W.H., Chiu, W.C. and Hsieh, W.H., 2006. Height effect on heat-transfer characteristics of aluminum-foam heat sinks. Journal of heat transfer, 128(6), pp.530-537.

25. Shih, W.H., Chou, F.C. and Hsieh, W.H., 2007. Experimental investigation of the heat transfer characteristics of aluminum-foam heat sinks with restricted flow outlet. Journal of Heat Transfer, 129(11), pp.1554-1563.
26. Feng, S.S., Kuang, J.J., Wen, T., Lu, T.J. and Ichimiya, K., 2014. An experimental and numerical study of finned metal foam heat sinks under impinging air jet cooling. International Journal of Heat and Mass Transfer, 77, pp.1063-1074.
27. Feng, S.S., Kuang, J.J., Lu, T.J. and Ichimiya, K., 2015. Heat transfer and pressure drop characteristics of finned metal foam heat sinks under uniform impinging flow. Journal of Electronic Packaging, 137(2), p.021014.
28. Wang, J., Kong, H., Xu, Y. and Wu, J., 2019. Experimental investigation of heat transfer and flow characteristics in finned copper foam heat sinks subjected to jet impingement cooling. Applied Energy, 241, pp.433-443.
29. Sung, H.C. and Liu, Y.H., 2017. Heat transfer in rectangular channels with porous wire mesh under impinging jet conditions. International Journal of Thermal Sciences, 122, pp.92-101.
30. Rallabandi, A.P., Rhee, D.H., Gao, Z. and Han, J.C., 2010. Heat transfer enhancement in rectangular channels with axial ribs or porous foam under through flow and impinging jet conditions. International Journal of Heat and Mass Transfer, 53(21-22), pp.4663-4671.
31. Singh, P., Zhang, M., Pandit, J. and Mahajan, R.L., 2018, November. Array Jet Impingement Onto High Porosity Thin Metal Foams at Zero Jet-to-Foam Spacing. In ASME 2018 International Mechanical Engineering Congress and Exposition (pp. V08BT10A020-V08BT10A020). American Society of Mechanical Engineers.

32. Madhavan, S., Singh, P. and Ekkad, S., 2019. Jet Impingement Heat Transfer Enhancement by Packing High-Porosity Thin Metal Foams Between Jet Exit Plane and Target Surface. Journal of Thermal Science and Engineering Applications, 11(6), p.061016.
33. Bhattacharya, A., Calmidi, V.V. and Mahajan, R.L., 2002. Thermophysical properties of high porosity metal foams. International Journal of Heat and Mass Transfer, 45(5), pp.1017-1031.
34. Lytle, D. and Webb, B.W., 1994. Air jet impingement heat transfer at low nozzle-plate spacings. International Journal of Heat and Mass Transfer, 37(12), pp.1687-1697.
35. Singh, P. and Ekkad, S.V., 2017. Effects of spent air removal scheme on internal-side heat transfer in an impingement-effusion system at low jet-to-target plate spacing. International Journal of Heat and Mass Transfer, 108, pp.998-1010.

CHAPTER 3

Conclusions and Recommendation for future work

The thesis presents an experimental study that characterizes flow distribution and heat transfer for thin metal foams subjected to array jet impingement for intermediate and maximum crossflow conditions. Metal foams offer large metal content to carry heat from the base plate that interacts with the impinging air and provide highly tortuous flow paths that leads to enhanced mixing. Increased local coolant velocity due to virtue of array jet impingement when combined with inherent properties of foams listed above, results in enhanced heat transfer. For 40 PPI foams, three different jet-to-target spacing (z/d=1, 2, 6) were investigated, and for a fixed jet-to-target spacing (z/d= 6), three different pore-density of 5, 20 and 40 PPI were investigated. The jet diameter-based Reynolds number was varied between 3,000 and 12,000. The following conclusions are drawn from the study.

1. For metal foam configurations, the jet mass flux distribution was highly non-uniform in comparison to that of the baseline configuration. This is attributed to the additional flow resistance imposed by the metal foams.
2. Jet impingement heat transfer for metal foams was primarily affected by the jet-to-target spacing, while the pore-density effect was secondary, with higher pore density yielding in higher heat transfer. This trend was observed for both the crossflow schemes.
3. The two lower jet-to-target spacings (z/d=1 and 2) had near-similar heat transfer levels, however, the pressure drop penalty for the lowest z/d was much higher than z/d=2. Hence the z/d=2 configuration had the higher thermal hydraulic performance in both exit crossflow conditions.

4. Thermal hydraulic performance of metal foams for intermediate crossflow condition was higher than the maximum crossflow.
5. The local heat transfer distribution was most uniform for the highest jet-to-target spacing (z/d=6), across all metal foam configurations as well as compared to the baseline configuration. However, the global heat transfer levels for z/d=6 was lower compared to the other two jet-to-target spacings for both metal foam and baseline configurations.
6. When heat transfer at constant pumping power was considered, the z/d=6 case was the best performing foam in maximum crossflow condition while z/d=2 performed the best under intermediate crossflow condition.

Future work could be on extrapolating the current study by validating it with a numerically developed code and accurately study heat transfer at the pore level. Since it is identified that enhancement occurs towards the end of the channel, there may exist more optimum configurations at lower jet-to-target spacings such as placing foams only at the ends or placing foams on the alternate rows which could reduce the pressure drop in the system without compromising significantly on the heat transfer enhancement.